Geophysical Research Letters

RESEARCH LETTER
10.1029/2018GL079742

Key Points:
- The space-time faulting history of the 4 May 2018 Hawaii Island earthquake is determined using seismic, geodetic, and tsunami data
- The earthquake generated a modest tsunami, well recorded around the Hawaiian islands, enabling hazard assessment for volcano flank events
- The tsunami impact along the Hawaiian Islands can be categorized at three regional levels in terms of peak wave amplitude and arrival time

Supporting Information:
- Supporting Information S1
- Movie S1

Correspondence to:
K. F. Cheung,
cheung@hawaii.edu

Citation:
Bai, Y., Ye, L., Yamazaki, Y., Lay, T., & Cheung, K. F. (2018). The 4 May 2018 M_w 6.9 Hawaii Island earthquake and implications for tsunami hazards. *Geophysical Research Letters*, *45*, 11,040–11,049. https://doi.org/10.1029/2018GL079742

Received 24 JUL 2018
Accepted 20 SEP 2018
Accepted article online 10 OCT 2018
Published online 20 OCT 2018

The 4 May 2018 M_w 6.9 Hawaii Island Earthquake and Implications for Tsunami Hazards

Y. Bai[1,2], L. Ye[3,4], Y. Yamazaki[2], T. Lay[5], and K. F. Cheung[2]

[1]Ocean College, Zhejiang University, Zhoushan, China, [2]Department of Ocean and Resources Engineering, University of Hawaii at Manoa, Honolulu, HI, USA, [3]Guangdong Provincial Key Lab of Geodynamics and Geohazards, School of Earth Sciences and Engineering, Sun Yat-sen University, Guangzhou, China, [4]Earthquake Research Institute, University of Tokyo, Tokyo, Japan, [5]Department of Earth and Planetary Sciences, University of California Santa Cruz, Santa Cruz, CA, USA

Abstract The 4 May 2018 (M_w 6.9) earthquake offshore of Kilauea Volcano has raised concerns about potential impacts of locally generated tsunamis in Hawaii. Iterative inversion of global seismic observations guided by forward modeling of regional geodetic and tsunami records yields a self-consistent fault slip model to quantify the physical processes. This earthquake, similar to other large events in the area, is found to involve a shallowly dipping thrust fault, plausibly on the décollement between the island volcanic edifice and the old Pacific seafloor. The uplift and seaward displacement of Kilauea's south flank generate a tsunami that wraps around Hawaii Island, exposing all shores to direct arrivals and the interconnected insular shelves to resonating wave activities. The impact along the Hawaiian Islands can be categorized at three regional levels in terms of peak wave amplitude and arrival time with implications for tsunami hazards from future larger earthquakes and flank failures.

Plain Language Summary On 4 May 2018, early in the 2018 Kilauea volcanic eruption sequence, an M_w 6.9 earthquake ruptured the south flank of Hawaii Island. The event involved seaward sliding of a wedge of the island offshore of the East Rift Zone, likely on the contact surface between the island and the Pacific Ocean seafloor. The resulting motion generated a modest tsunami that arrived on the shores of the major Hawaiian Islands in less than an hour. The short time before the tsunami arrival prompted concerns about response planning for potential larger earthquakes on Kilauea's flank. A model of the earthquake rupture is determined using teleseismic waves, geodetic records, and tsunami observations. Numerical modeling of the tsunami propagation along the island chain reveals coastal regions with severe, moderate, and minor impact. The earthquake parameters, rupture extent, and tsunami impact from this study are useful for local tsunami hazard assessment and mitigation.

1. Introduction

An M_w 6.9 earthquake struck the south flank of Kilauea Volcano, Hawaii Island on 4 May 2018 (22:32:54 UTC; 19.313°N, 154.998°W, depth 2.1 ± 3.6 km; U.S. Geological Survey [USGS] National Earthquake Information Center: https://earthquake.usgs.gov/earthquakes/eventpage/us1000dyad#executive). The rupture produced a modest, but well-recorded tsunami at water-level stations around the Hawaiian Islands (see Figure 1 for locations). The tsunami reached 0.36- and 0.11-m elevation at the Kapoho and Honuapo stations, maintained by the Pacific Tsunami Warning Center (PTWC), northeast and southwest of the epicenter, and −0.24 and 0.16 m at the Hilo and Kawaihae tide gauges around the island. The waves maintained 0.15-m amplitude at Kahului, Maui before rapidly reducing to 0.03 m at Honolulu, Oahu and 0.04 m at Nawiliwili, Kauai. The event, which was essentially a scaled-down version of the M_w 7.7 Kalapana earthquake in 1975 (e.g., Ando, 1979; Furumoto & Kovach, 1979), has reignited concerns about tsunamis from Kilauea flank deformation and the level of potential impacts along the island chain.

The 4 May 2018 earthquake occurred early in the 2018 Kilauea eruption sequence, the day after fissure eruptions commenced in Leilani Estates. The hypocenter is located immediately offshore of the East Rift Zone, and a point-source solution with northwestward 20°-dipping thrust faulting was determined by the USGS (https://earthquake.usgs.gov/earthquakes/eventpage/us1000dyad#executive). The hypocenter and long-period faulting mechanism are similar to those of the 1975 Kalapana earthquake (e.g., Nettles & Ekström, 2004), which induced significant coastal slumping and produced a much larger local tsunami (e.g., Gillard et al., 1996; Ma et al., 1999). The 1975 rupture is generally accepted to involve thrusting on the décollement

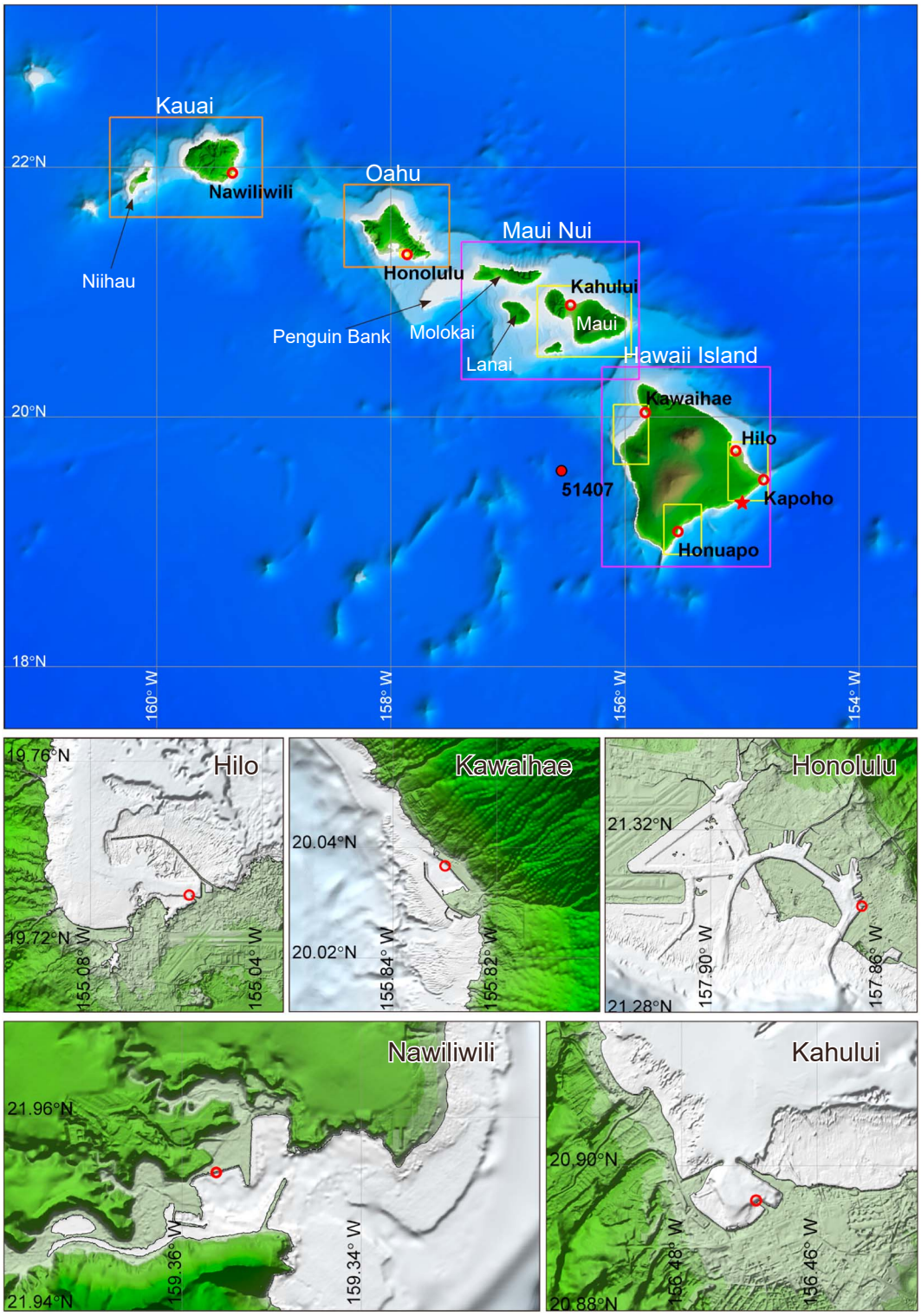

Figure 1. Location maps, digital elevation models, and nested computational grids. (top) Level 1 grid at 24-arcsec resolution and layout of level 2 and 3 grids. The orange and purple rectangles delineate level 2 grids at 3 and 6 arcsec, and the yellow color denotes level 3 grids at 3-arcsec resolution. (bottom panels) Level 3 and 4 grids at 0.3-arcsec resolution for harbors with tide stations. The red solid circle denotes the DART station, the open red circles represent tide and water-level stations, and the red star is the earthquake epicenter.

underlying the volcanic edifice (e.g., Furumoto & Kovach, 1979; Morgan et al., 2000), but slumping may have contributed to the tsunami excitation (e.g., Day et al., 2005; Ma et al., 1999). Such events have shown a pattern of recurrence. The great 1868 Kau earthquake in southern Hawaii Island is also thought to involve décollement rupture (Wyss, 1988).

The 2018 event provides a valuable case study with well-recorded geophysical and hydrographic data sets to examine local tsunami hazards from seismic activities on the south flank of Kilauea Volcano. We reconstruct the earthquake source mechanism through finite fault inversion of global seismic waves guided by forward modeling of geodetic records on Hawaii Island and tsunami measurements along the island chain. The joint analysis, which takes advantage of the diverse spatial and temporal scales of the observations, can resolve the faulting geometry and slip distribution and account for the tsunami excitation (e.g., Bai et al., 2017; Heidarzadeh et al., 2016; Gusman et al., 2017; Yamazaki et al., 2011). The modeled tsunami allows examination of the propagation and attenuation of waves generated on southeast Hawaii Island to the rest of the island chain in support of emergency response planning.

2. Methodology

We utilize an iterative inversion and forward modeling approach to estimate the kinematic space-time history of fault slip for the 2018 Hawaii Island earthquake and the resulting tsunami along the Hawaiian Island chain. Long-period *W*-phase moment-tensor inversions (e.g., Kanamori & Rivera, 2008; Figure S1 in the supporting information) and fitting of long-period Love wave spectra provide initial estimates of the faulting geometry for the kinematic finite-fault inversions (e.g., Hartzell & Heaton, 1983; Lay et al., 2018; Ye et al., 2016; Text S1 in the supporting information). The very shallow source in this case results in variation of the estimated strike (226° to 240°) and dip (2.5° to 20°), so a range of model geometries is considered. We further constrain the fault dip to be in the range of 2.5° to 7.5°, adopting a preferred value of 7.5°, based on fitting of long-period Love wave radiation patterns, which are particularly sensitive to the fault dip (Figure S2). Our broadband teleseismic data set of 79 *P* wave ground displacements and 43 *SH* wave ground velocities have limited resolution of the fault geometry and slip due to the small size of the event. Predicted surface displacements for each model using Okada (1985) are compared with coseismic Global Positioning System (GPS) displacements along the southeast shore of Hawaii Island to help constrain the fault geometry. The GPS data from continuously operating stations in the area were processed by the Nevada Geodetic Laboratory, the University of Nevada, Reno using JPL's GIPSY software and rapid orbit products. Automatically produced 5-min position time series were used to estimate coseismic offsets from 57 stations near the epicenter.

The promising fault slip models are used to define the kinematic seafloor deformation for modeling the tsunami waves at the PTWC Kapoho and Honuapo stations on the southeast shore fronting the tsunami source, as well as at DART 51407 at 4,771-m water depth off west Hawaii Island (see Figure 1). Comparison with the recorded data provides additional guidance for refinement of the source parameters in a new round of finite fault inversions. The complex time functions in the subfaults are replaced by the cumulative moment, average rake, and total rise time for tsunami modeling. The nonhydrostatic model, NEOWAVE (Yamazaki et al., 2009; Yamazaki et al., 2011), is used to compute the tsunami generated by the seafloor motion and its propagation along the island chain. The shock-capturing finite difference model augments the nonlinear shallow-water equations with a depth-averaged vertical velocity term to describe nonhydrostatic flows over steep volcanic slopes and wave dispersion during propagation. The vertical velocity term also enables modeling of tsunami generation with a kinematic seafloor boundary condition derived from a finite-fault model and corrected for local slopes using the approach of Tanioka and Satake (1996). These features are essential for modeling of near-field tsunami waves that are strongly influenced by the generation mechanism and the steep local bathymetry.

The tsunami modeling requires up to four levels of two-way nested spherical grids to resolve multiscale wave processes from the earthquake source to the coastal water-level stations. The digital elevation model includes multibeam, LiDAR, and hydrographic survey data sets with 1- to 50-m resolution. Figure 1 shows the level 1 grid with 24-arcsec (~740 m at Hawaii's latitude) resolution across the Hawaiian Islands and the layout of the nested grid systems. The level 2 grids resolve the insular slopes and shelves at 6 arcsec (~185 m) for Hawaii and Maui Islands and 3 arcsec (~92.5 m) for Oahu, Kauai, and Niihau. An intermediate level of grids brings the resolution of Hawaii and Maui Island's shores to 3 arcsec (~92.5 m). The tsunami

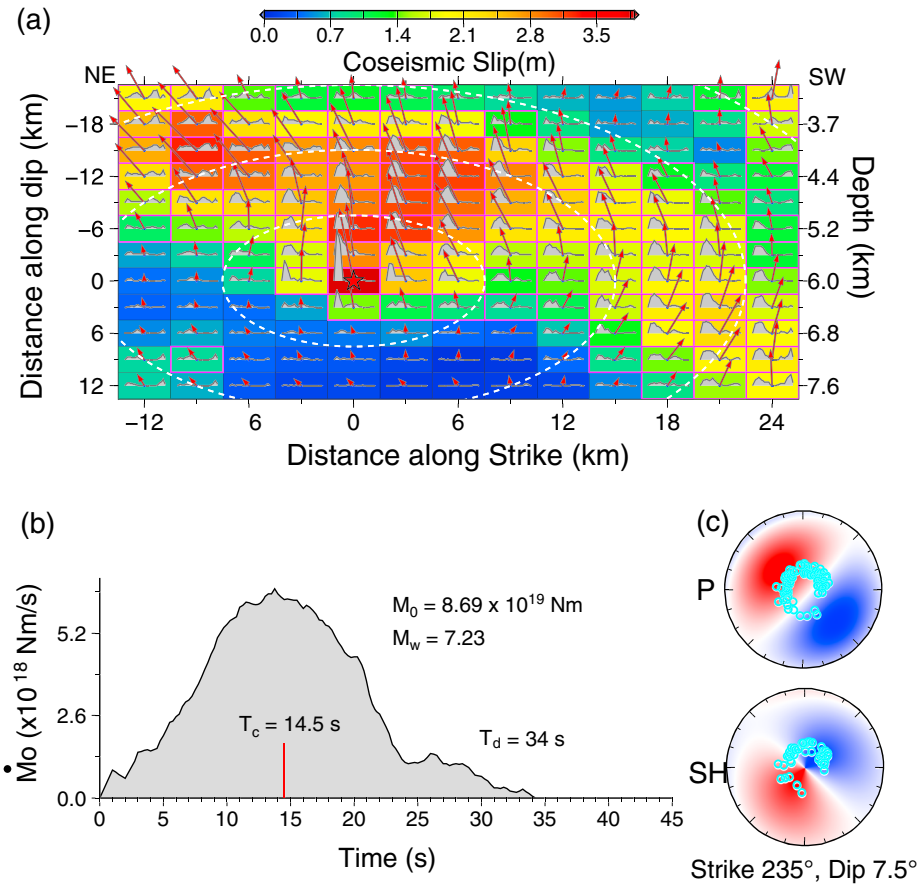

Figure 2. Preferred fault model constrained by inversion of teleseismic broadband data (Figure S3) and forward modeling of nearby Global Positioning System offsets (Figures 3c and 3d) and tsunami recordings (Figure 4a). (a) The subfault average rake (arrows, in the fault plane) and slip (color-coded and proportional to the length of arrows). The white dashed curves are 5-s increments of the rupture front expansion position for the 1.5-km/s average velocity. (b) The moment rate function indicates a total duration T_d ~34 s, with a centroid time T_c ~14.5 s. (c) The focal mechanisms show the distribution of teleseismic *P* and *SH* data used in the inversion.

signals at the Kapoho and Honuapo stations, which are located on rugged volcanic shores, are computed with this resolution due to the lack of detailed bathymetry in their vicinity. The finest grids at levels 3 or 4 cover 6 to 10 km of shorelines at Hilo, Kawaihae, Kahului, Honolulu, and Nawiliwili to capture the reefs and channels at 0.3-arcsec (~9 m) resolution for validation of the model results with the tide gauge signals. A Manning coefficient of 0.035 (s $m^{-1/3}$) describes subgrid roughness for the nearshore reefs and the volcanic substrates of Hawaii (Bretschneider et al., 1986).

3. The Earthquake and Tsunami Models

The preferred model in Figure 2 produces good matches to the teleseismic body waves with normalized residual waveform power of 0.20 (Figure S3). The rupture duration is ~34 s, and the kinematic rupture expansion speed is 1.5 km/s. The subfaults are 3 km × 3 km with durations of up to 13 s. The relatively low rupture expansion speed is needed even for the relatively long subfault durations largely due to the need for source compactness in matching the GPS and tsunami observations. The tsunami arrival time at Kapoho and the initial waveform at DART 51407, along with the azimuthal convergence in the GPS vectors (Figure 3d), further constrain the along strike fault dimension to 39 km. The model is not able to reproduce the arrival time at Honuapo within the plausible range of fault dimensions likely due to the location of the sensor in a stilling well plagued by algae growth. Peak slip is about 3.8 m, with a large slip patch located from 3.7 to 6.4 km deep. The strike is 235° and the seismic moment M_0 is 8.7 × 10^{19} Nm (M_w 7.2). The moment magnitude is increased

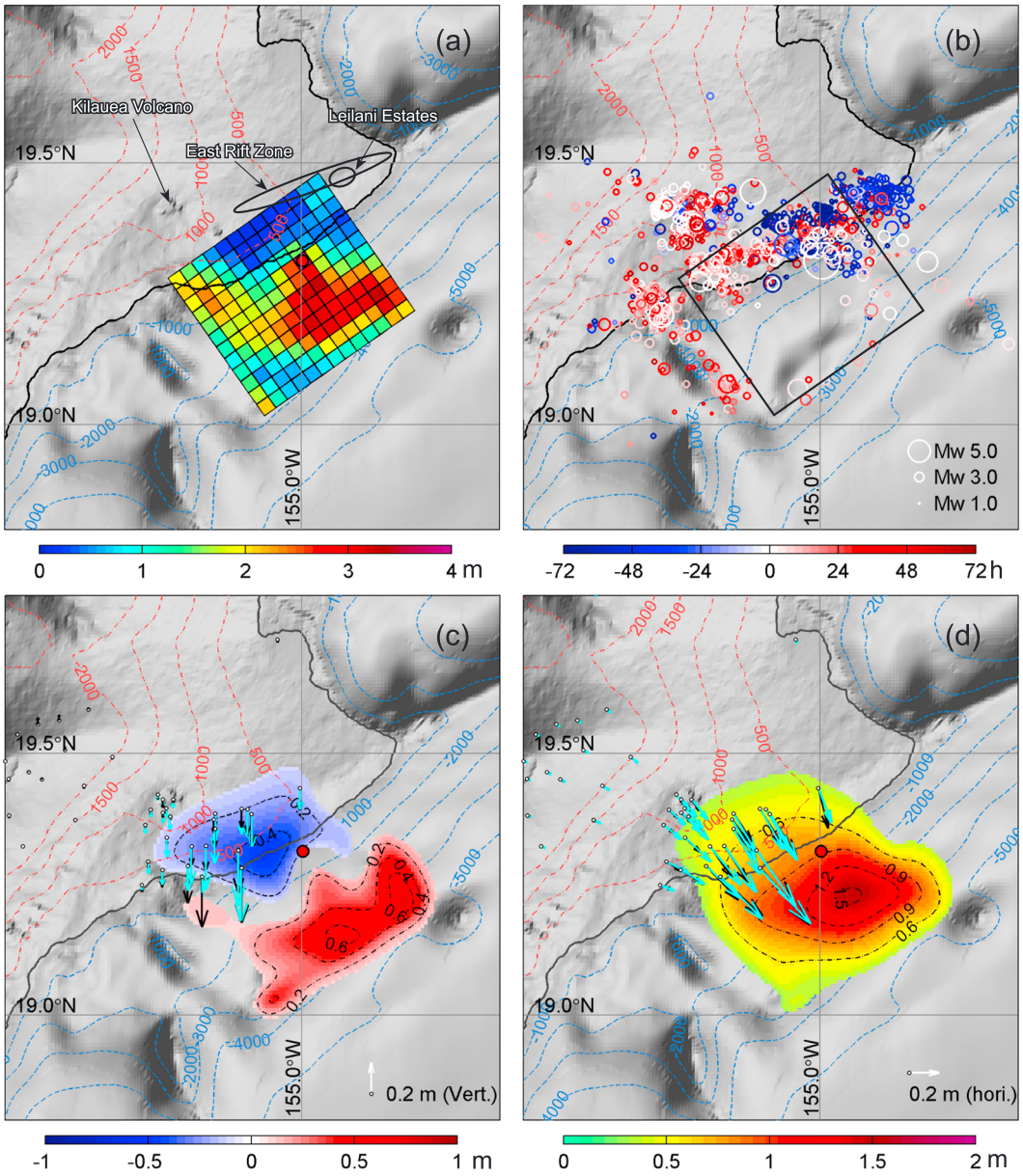

Figure 3. Comparison of the preferred fault model with observations. (a) Co-seismic slip in map view. (b) Seismicity from the USGS National Earthquake Information Center catalog, color-coded by earthquake time relative to the M_w 6.9 main shock. (c) Vertical surface displacement. (d) Horizontal surface displacement. The red solid circle in (a), (c), and (d) identifies the earthquake epicenter. The black and cyan arrows in (c) and (d) denote predicted and observed Global Positioning System vectors. The dashed contours show topography (red) and bathymetry (blue) with 500- and 1,000-m intervals.

from the USGS estimate due to the shallower fault dip δ, as the excitation of long-period surface waves varies proportional to $M_0 \sin(2\delta)$ for such a shallow dip-slip event (Text S2; Kanamori & Given, 1981). The slip-weighted, average static stress drop for this model is 6.3 MPa using the method of Ye et al. (2016; Figure S4). The corresponding radiated seismic energy and the moment-scaled value are $E_R = 4.3 \times 10^{14}$ J and $E_R/M_0 = 5.42 \times 10^{-6}$ (Figure S5). The low rupture expansion velocity and moment-scaled radiated energy are similar to values for shallow, shallowly dipping tsunami earthquakes in subduction zones (e.g., Ye et al., 2016).

The preferred model has strong correlation with seismicity and geodetic observations on southeast Hawaii Island. Figures 3a and 3b show the large slip patch located offshore on the steep insular slope roughly

parallel to the East Rift Zone and surrounded by foreshocks and aftershocks during 3 days before and 3 days after the M_w 6.9 main shock. The slip distribution is similar to an inversion of teleseismic, strong motion, and GPS recordings by Liu et al. (2018). The main foreshocks and aftershocks extend parallel to the shore along the active fissure distribution in the East Rift Zone, with secondary trends extending perpendicular to the shore southwest and northeast of the rupture zone. Sparse activity occurs along the updip boundary of the model. The area of large-slip has very low seismicity, as commonly observed for large subduction zone events (Wetzler et al., 2018; Yamazaki et al., 2018). The seafloor vertical and horizontal displacements in Figures 3c and 3d fit the regional coseismic GPS static motions satisfactorily. The model results show subsidence of up to 0.5 m at the shore, uplift reaching 0.7 m on the insular slope, and seaward displacement of Kilauea's south flank by as much as 1.5 m. The corresponding time history of seafloor deformation defines the kinematic boundary condition for modeling of the tsunami.

Movie S1 in the supporting information illustrates the generation of the tsunami at the source and propagation around the Hawaiian Islands. The seafloor uplift and horizontal displacement on the steep slope generate a slightly oblong initial sea-surface pulse of ~1-m amplitude, which, during its descent, splits into two nearly overlapping systems of radial waves. The compact initial pulse and the relatively large water depth give rise to notable nonhydrostatic characteristics of the resulting sea-surface motion with a deep downswing. The enduring oscillations generate a series of waves with decreasing amplitude from the source. The steep volcanic slope and the absence of a shelf facilitate onshore propagation of the tsunami and wrap-around of the waves to the west and northeast-facing shores before converging at the northern tip of Hawaii Island. At about the same time, the faster propagating offshore waves reach Maui Nui, the interconnected shelves of Maui, Molokai, and Lanai, from the north and south. The shallow shelves trap a significant amount of energy from the tsunami as standing edge waves, reducing its amplitude along the rest of the island chain to the northwest. The longer-period trapped waves over Maui Nui are leaked to Oahu via the 50-m deep Penguin Bank as seen in modeled tsunamis originating from the Pacific Rim (e.g., Munger & Cheung, 2008; Yamazaki et al., 2012). The insular shelves of Kauai and Niihau are narrow and disconnected from the rest of the islands. The tsunami excitation is primarily from the offshore propagation, which is noticeably attenuated due to the distance from the source.

Figure 4 compares the computed waveforms and spectra with the recorded signals at the DART, PTWC, and tide stations. The DART record is helpful in constraining the along-strike rupture dimension. The two radial wave systems from the source lead to the double-peak feature as seen in the computed and recorded initial arrivals around 0.35 hr. Increasing the along-strike fault dimension to the east or west or using a higher kinematic rupture expansion velocity leads to increased separation of the double peaks, degrading the fit to the record (see Figure S6). The large trough, which is influenced to a lesser extent by the shape of the uplift patch, is well accounted for by the nonhydrostatic computation. The arrival time at Kapoho provides a more direct constraint on the eastern extent of the model rupture. The slight mismatch of the computed initial peak is due to inadequate resolution of the nearshore bathymetry. The preferred model is validated using tsunami records from five tide gauges that were not used in its iterative refinement. The oscillations over the insular shelves of Hawaii are primarily governed by a series of resonance modes, as demonstrated by Cheung et al. (2013). This is evident in the belated arrival of the peak-amplitude wave even at Hilo and Kawaihae immediately on the leeside of the source and the persistent oscillations at Kahului over Maui Nui. The good agreement between the computed and recorded signals over an extended duration indicates reproduction of the spectral content and phase in the tsunami excitation. The model also reproduces the initial arrivals at Honolulu and Nawiliwili in spite of the weak tsunami signals amidst comparable background oscillations.

The sea-surface elevation time series show significant variation of the tsunami waves along the island chain. Figure 5 plots the maximum elevation as well as the arrival time of the initial and largest peaks to provide insight into the local tsunami hazards. Southeast Hawaii Island is the hardest hit due to the direct approach and simultaneous reflection of the initial sea-surface pulse. The tsunami waves attenuate considerably along the shores outside the rupture zone. The wrap-around waves have secondary impacts on the west and northeast-facing shores of Hawaii Island. A similar level of impact extends to the shores of Maui, Lanai, and Molokai due to waves approaching from both sides of the island chain and trapping of edge waves. The nearshore wave amplitude reduces significantly on Oahu and Kauai leeward of Maui Nui, which acts as a trap of the tsunami waves propagating along the island chain (see Movie S1). The arrival time of the initial peak follows the celerity and travel distance. The results show near-instant arrival on southeast Hawaii Island

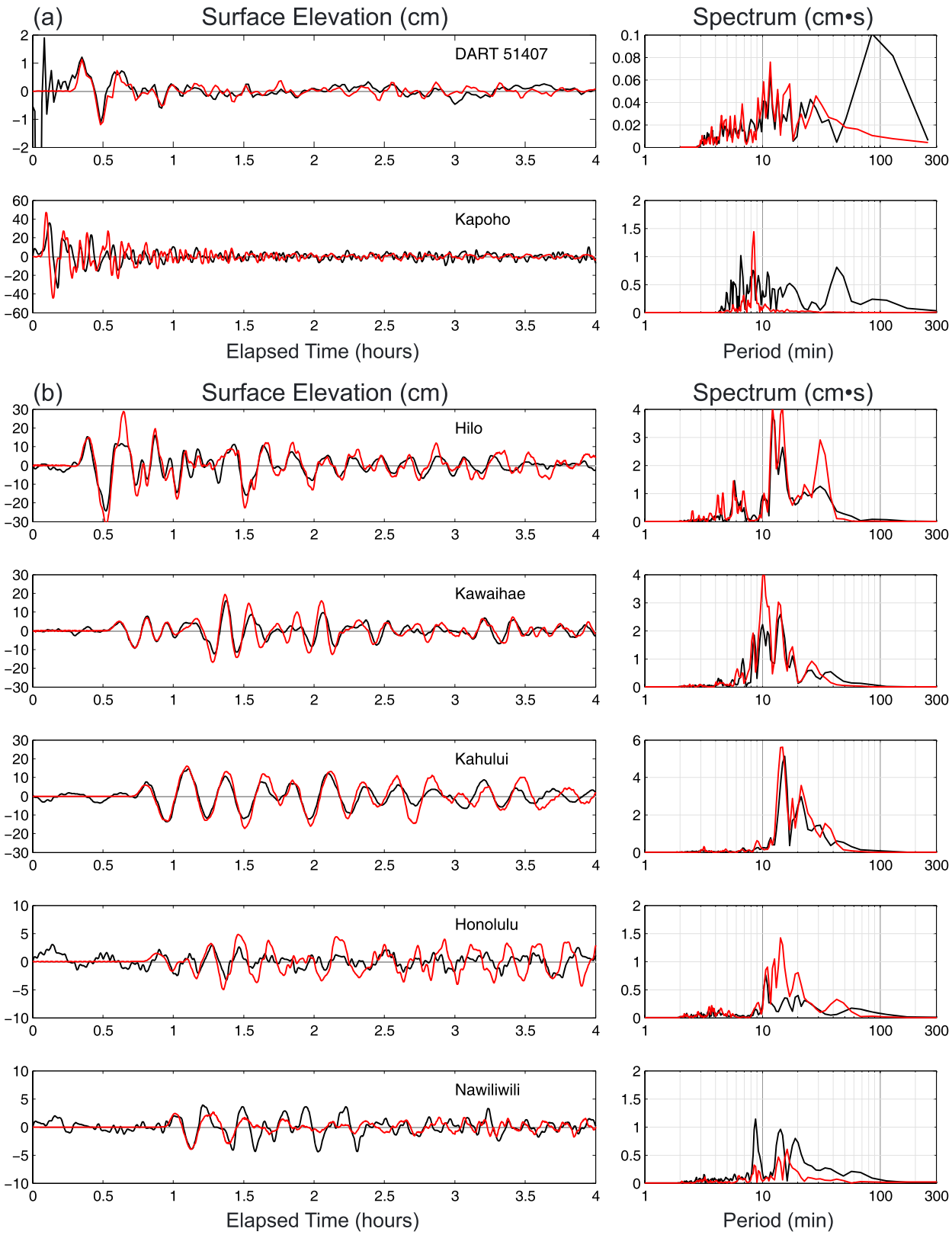

Figure 4. Comparison of water-level records (black lines) with computed waveforms and spectra (red lines) from the preferred fault model. (a) Water-level stations used in iterative refinement. (b) Tide stations for model validation.

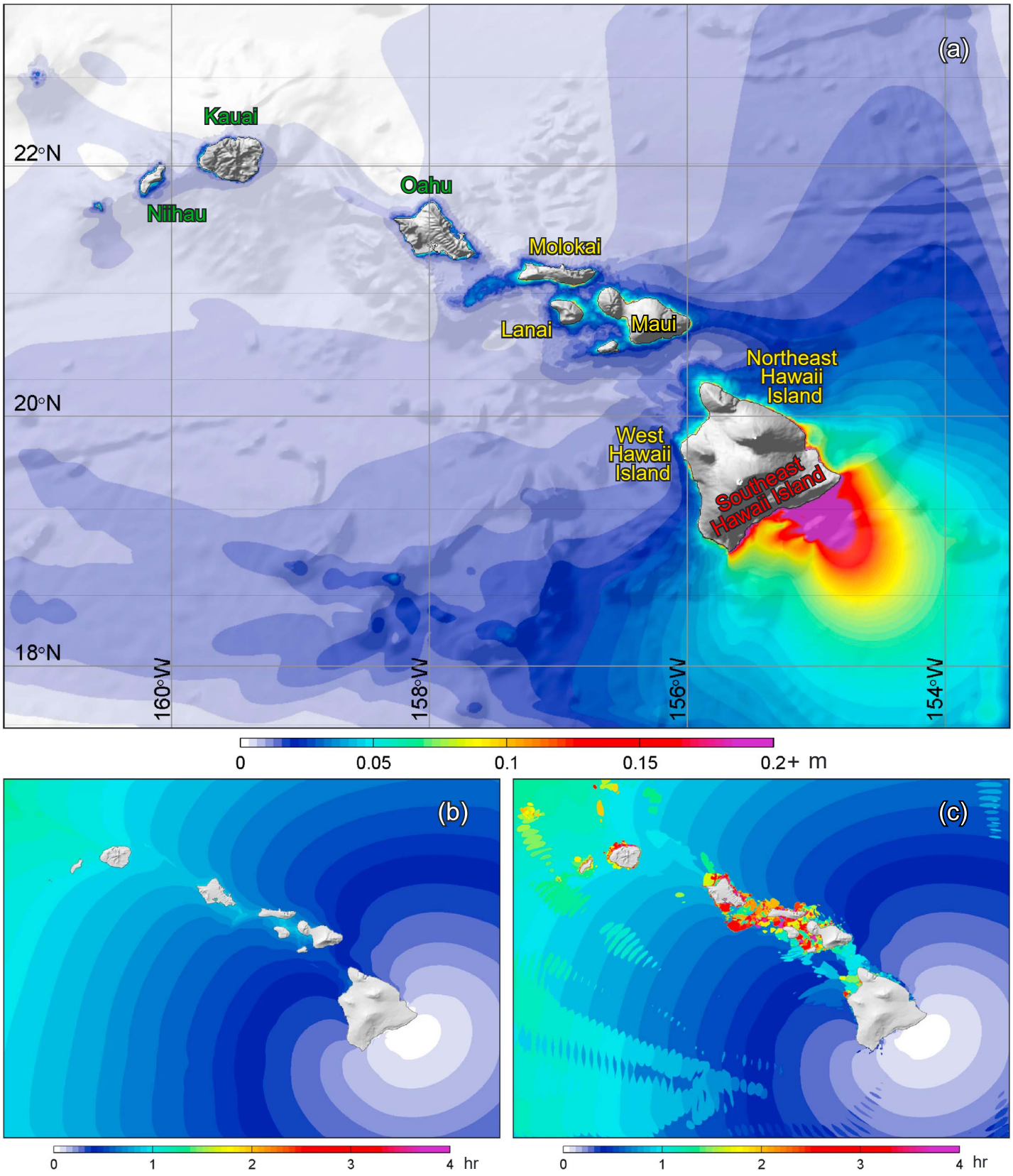

Figure 5. Tsunami impacts along the Hawaiian island chain from the preferred fault model. (a) Maximum wave amplitude. Island names or shores are color-coded as red, yellow, and green to indicate decreasing level of impact. (b) Arrival time of initial peak. (c) Arrival time of largest peak.

due to the steep drop off and a slight delay along the island chain from the adjacent deep water caused by lower celerity on the insular shelves. The initial peak reaches all major Hawaiian Islands within an hour. The largest wave, however, can appear locally up to 4 hr after the earthquake. These belated peak arrivals occur mostly at locations with wide insular shelves due to constructive interference of trapped edge waves. Scattering of tsunami waves by seamounts also results in late arrival of the largest peak across the open ocean (Bai et al., 2015).

4. Discussion and Conclusions

The 4 May 2018 Hawaii Island earthquake is a manifestation of the seaward sliding of the south flank of Kilauea. Injection of magma into the East Rift Zone clearly contributes to some pressure on the wedge of material driving the seaward displacement, but it is important to recognize that most of the magmatic injection (drained from the Kilauea summit) occurred after the earthquake. The topographic stress on the mountain, combined with an apparently weakly coupled décollement, also provides a mechanism for lateral spreading of the volcano flanks, particularly along the young southeastern side of the island. The 1975 Kalapana earthquake was much larger and not directly linked to simultaneous magma injection along the East Rift Zone, so triggering of large earthquake faulting on the décollement does not require additional synchronous forcing. The 2018 event may have actually enhanced the rifting, with extensional stress along the rift zone being increased by the seaward thrusting. While cause and effect can be debated, there seems to be no question that the earthquake is intrinsically related to the 2018 eruption sequence. There will likely be future events similar to the 1975 Kalapana earthquake and tsunami as the island flank accommodates further rifting.

A locally generated tsunami is of particular concern to emergency management agencies in Hawaii because of its short arrival time and unforeseeable amplitude along the island chain. The validated model results for the 2018 event provide a proxy to develop a response strategy for future tsunamis from the south flank of Kilauea. The tsunami impact along the Hawaiian Island chain can be categorized at three regional levels in terms of the peak wave amplitude and arrival time. The model results show highly localized and almost instantaneous impact along the southeast shore of Hawaii Island. The wave amplitude is significantly reduced to a similar level for the west and northeast shores of the island and for Maui, Lanai, and Molokai, but coastal currents can remain considerable over the reefs despite the reduced wave amplitude at the shore (Bai & Cheung, 2016). Oahu and Kauai further west sustain an even lower level of wave action. However, the largest nearshore wave might appear hours after the initial arrival at locations from north Hawaii Island to Kauai, wherever wide insular shelves are present.

The modeling of the 2018 event is the first step to assess potential hazards posed by locally generated tsunamis in Hawaii. Additional modeling of tsunamis generated by earthquakes comparable to the 1975 Kalapana event along the southeast shore of Hawaii Island is currently underway. The model results will enable delineation of inundation zones for evacuation planning and maritime hazard maps for harbor operations assessment. PTWC presently utilizes a threshold of M_w 7.5 for warning of Hawaii and Maui Islands in the event of a southeast Hawaii Island earthquake. The warning will be extended to the entire state if its gauge network indicates over 3 m of wave amplitude or runup. Rapid determination of faulting parameters from global seismic observations and regional GPS measurements will be valuable to improve the initial magnitude estimate. The three regional levels of potential impact identified in this study will be substantiated by modeling of 1975-type events to provide additional granularity for response planning utilizing a combination of advisory and warning across the state.

Acknowledgments
This study utilized GMT for digital elevation model development and Matlab for data analysis and presentation. The Incorporated Research Institutions for Seismology (IRIS) data management service (DMS) was used to access the seismic data, while the GPS coseismic displacement data were obtained from the Nevada Geodetic Laboratory (NGL, http://geodesy.unr.edu/). The recorded tide gauge and DART data were obtained from the National Data Buoy Center at http://www.ndbc.noaa.gov/. We would like to thank Stuart Weinstein for providing water-level records from stations maintained by the Pacific Tsunami Warning Center, Hiroo Kanamori for sharing with us a W-phase solution at the start of this research, and Kenji Satake, Gerard Fryer, Stuart Weinstein, Paul Okubo, Gavin Hayes (the Editor), and the two anonymous reviewers for the helpful comments on the manuscript. The National Oceanic and Atmospheric Administration supported this study through grant NA17NWS4670012 via Hawaii Emergency Management Agency to Kwok Fai Cheung and Yoshiki Yamazaki and the National Science Foundation through grant EAR1802364 to Thorne Lay. The Junior Thousand Talents Plan of China and the 100 Talents program of Sun Yat-sen University provided support to Lingling Ye. SOEST contribution 10445.

References

Ando, M. (1979). The Hawaii Earthquake of November 29, 1975: Low dip angle faulting due to forced injection of magma. *Journal of Geophysical Research*, *84*(B13), 7616–7626. https://doi.org/10.1029/JB084iB13p07616

Bai, Y., & Cheung, K. F. (2016). Hydrostatic versus non-hydrostatic modeling of tsunamis with implications for insular shelf and reef environments. *Coastal Engineering*, *117*, 32–43. https://doi.org/10.1016/j.coastaleng.2016.07.008

Bai, Y., Lay, T., Cheung, K. F., & Ye, L. (2017). Two regions of seafloor deformation generated the tsunami for the 13 November 2016, Kaikoura, New Zealand earthquake. *Geophysical Research Letters*, *44*, 6597–6606. https://doi.org/10.1002/2017GL073717

Bai, Y., Yamazaki, Y., & Cheung, K. F. (2015). Interconnection of multi-scale standing waves across the Pacific from the 2011 Tohoku tsunami. *Ocean Modelling*, *92*, 183–197. https://doi.org/10.1016/j.ocemod.2015.06.007

Bretschneider, C. L., Krock, H. J., Nakazaki, E., & Casciano, F. M. (1986). Roughness of typical Hawaiian terrain for tsunami run-up calculations: A user's manual. J.K.K. Look Lab. Rep., Univ. of Hawaii, Honolulu.

Cheung, K. F., Bai, Y., & Yamazaki, Y. (2013). Surges around Hawaiian Islands from the 2011 Tohoku tsunami. *Journal of Geophysical Research: Oceans*, *118*, 5703–5719. https://doi.org/10.1002/jgrc.20413

Day, S. J., Watts, P., Grilli, S. T., & Kirby, J. T. (2005). Mechanical models of the 1975 Kalapana, Hawaii earthquake and tsunami. *Marine Geology*, *215*(1–2), 59–92. https://doi.org/10.1016/j.margeo.2004.11.008

Furumoto, A. S., & Kovach, R. L. (1979). The Kalapana earthquake of November 29, 1975: An intra-plate earthquake and its relation to geothermal processes. *Physics of the Earth and Planetary Interiors*, *18*(3), 197–208. https://doi.org/10.1016/0031-9201(79)90114-6

Gillard, D., Wyss, M., & Okubo, P. (1996). Type of faulting and orientation of stress and strain as a function of space and time in Kilauea's south flank, Hawaii. *Journal of Geophysical Research*, *101*, 16,025–16,042. https://doi.org/10.1029/96JB00651

Gusman, A. R., Satake, K., & Harada, T. (2017). Rupture process of the 2016 Wharton Basin strike-slip faulting earthquake estimated from joint inversion of teleseismic and tsunami waveforms. *Geophysical Research Letters*, *44*, 4082–4089. https://doi.org/10.1002/2017GL073611

Hartzell, S. H., & Heaton, T. H. (1983). Inversion of strong ground motion and teleseismic waveform data for the fault rupture history of the 1979 Imperial Valley, California earthquake. *Bulletin of the Seismological Society of America*, *73*(6A), 1553–1583.

Heidarzadeh, M., Murotani, S., Satake, K., Ishibe, T., & Gusman, A. R. (2016). Source model of the 16 September 2015 Illapel, Chile, M_W 8.4 earthquake based on teleseismic and tsunami data. *Geophysical Research Letters*, *43*, 643–650. https://doi.org/10.1002/2015GL067297

Kanamori, H., & Given, J. W. (1981). Use of long-period surface waves for rapid determination of earthquake-source parameters. *Physics of the Earth and Planetary Interiors*, *27*(1), 8–31. https://doi.org/10.1016/0031-9201(81)90083-2

Kanamori, H., & Rivera, L. (2008). Source inversion of W phase: Speeding up seismic tsunami warning. *Geophysical Journal International*, *175*(1), 222–238. https://doi.org/10.1111/j.1365-246X.2008.03887.x

Lay, T., Ye, L., Kanamori, H., and Satake, K. (2018). Constraining the dip of shallow, shallowly-dipping thrust events using long-period Love wave radiation patterns: Application to the 25 October 2010 Mentawai, Indonesia and 4 May 2018 Hawaii Island earthquakes. *Geophysical Research Letters*, *45*. https://doi.org/10.1029/2018GL080042

Liu, C., Lay, T., & Xiong, X. (2018). Rupture in the 4 May 2018 M_W 6.9 earthquake seaward of the Kilauea East Rift Zone fissure eruption in Hawaii. *Geophysical Research Letters*, *45*. https://doi.org/10.1029/2018GL079349

Ma, K.-F., Kanamori, H., & Satake, K. (1999). Mechanism of the 1975 Kalapana, Hawaii earthquake inferred from tsunami data. *Journal of Geophysical Research*, *104*, 13,153–13,167. https://doi.org/10.1029/1999JB900073

Morgan, J. K., Moore, G. F., Hills, D. J., & Leslie, S. (2000). Overthrusting and sediment accretion along Kilauea's mobile south flank, Hawaii: Evidence for volcanic spreading from marine seismic reflection data. *Geology*, *28*(7), 667–700. https://doi.org/10.1130/0091-7613(2000)28<667:OASAAK>2.0.CO;2

Munger, S., & Cheung, K. F. (2008). Resonance in Hawaii waters from the 2006 Kuril Islands tsunami. *Geophysical Research Letters*, *35*, L07605. https://doi.org/10.1029/2007GL032843

Nettles, M., & Ekström, G. (2004). Long-period source characteristics of the 1975 Kalapana, Hawaii, earthquake. *Bulletin of the Seismological Society of America*, *94*(2), 422–429. https://doi.org/10.1785/0120030090

Okada, Y. (1985). Surface deformation due to shear and tensile faults in a half-space. *Bulletin of the Seismological Society of America*, *75*(4), 1135–1154.

Tanioka, Y., & Satake, K. (1996). Tsunami generation by horizontal displacement of ocean bottom. *Geophysical Research Letters*, *23*, 861–864. https://doi.org/10.1029/96GL00736

Wetzler, N., Lay, T., Brodsky, E. E., & Kanamori, H. (2018). Systematic deficiency of aftershocks in areas of high coseismic slip for large subduction zone earthquakes. *Science Advances*, *4*(2), eaao3225. https://doi.org/10.1126/sciadv.aao3225

Wyss, M. (1988). A proposed source model for the great Kau, Hawaii, earthquake of 1868. *Bulletin of the Seismological Society of America*, *78*(4), 1450–1462.

Yamazaki, Y., Cheung, K. F., & Kowalik, Z. (2011). Depth-integrated, non-hydrostatic model with grid nesting for tsunami generation, propagation, and run-up. *International Journal for Numerical Methods in Fluids*, *67*(12), 2081–2107. https://doi.org/10.1002/fld.2485

Yamazaki, Y., Cheung, K. F., & Lay, T. (2018). A self-consistent fault-slip model for the 2011 Tohoku earthquake and tsunami. *Journal of Geophysical Research: Solid Earth*, *123*, 1425–1458. https://doi.org/10.1002/2017JB014749

Yamazaki, Y., Cheung, K. F., Pawlak, G., & Lay, T. (2012). Surges along the Honolulu coast from the 2011 Tohoku tsunami. *Geophysical Research Letters*, *39*, L09604. https://doi.org/10.1029/2012GL051624

Yamazaki, Y., Kowalik, Z., & Cheung, K. F. (2009). Depth-integrated, non-hydrostatic model for wave breaking and run-up. *International Journal for Numerical Methods in Fluids*, *61*(5), 473–497. https://doi.org/10.1002/fld.1952

Yamazaki, Y., Lay, T., Cheung, K. F., Yue, H., & Kanamori, H. (2011). Modeling near-field tsunami observations to improve finite-fault slip models for the 11 March 2011 Tohoku earthquake. *Geophysical Research Letters*, *38*, L00G15. https://doi.org/10.1029/2011GL049130

Ye, L., Lay, T., Kanamori, H., & Rivera, L. (2016). Rupture characteristics of major and great ($M_W \geq 7$) megathrust earthquake from 1990-2015: 1. Moment scaling relationships. *Journal of Geophysical Research: Solid Earth*, *121*, 821–844. https://doi.org/10.1002/2015JB012426